NANO LETTERS

LETTER

pubs.acs.org/NanoLett

Bottom-up Photonic Crystal Lasers

Adam C. Scofield,*,† Se-Heon Kim,‡ Joshua N. Shapiro,† Andrew Lin,† Baolai Liang,† Axel Scherer,‡ and Diana L. Huffaker*,†

†Department of Electrical Engineering and California NanoSystems Institute, University of California at Los Angeles, Los Angeles, California 90095, United States

‡Department of Electrical Engineering and Kavli Nanoscience Institute, California Institute of Technology, Pasadena, California 91125, United States

Supporting Information

ABSTRACT: The directed growth of III−V nanopillars is used to demonstrate bottom-up photonic crystal lasers. Simultaneous formation of both the photonic band gap and active gain region is achieved via catalyst-free selective-area metal−organic chemical vapor deposition on masked GaAs substrates. The nanopillars implement a GaAs/InGaAs/GaAs axial double heterostructure for accurate, arbitrary placement of gain within the cavity and lateral InGaP shells to reduce surface recombination. The lasers operate single-mode at room temperature with low threshold peak power density of ~625 W/cm^2. Cavity resonance and lasing wavelength is lithographically defined by controlling pillar pitch and diameter to vary from 960 to 989 nm. We envision this bottom-up approach to pillar-based devices as a new platform for photonic systems integration.

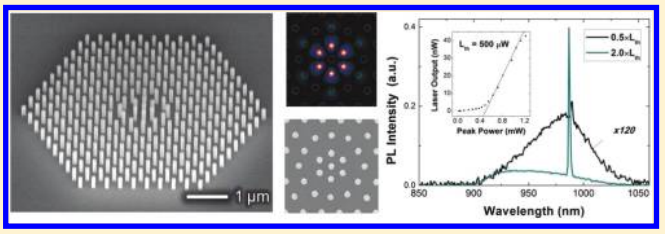

KEYWORDS: Nanopillar, nanowire, photonic crystal laser, low threshold

In the past decade, intense research has been performed in the area of nanowires (NWs) and nanopillars (NPs). These semiconductor nanostructures can be synthesized with specific material compositions,[1] axial and radial heterostructures,[2,3] and on large lattice mismatched substrates including silicon.[4,5] Such attributes, combined with their small cross sections, promise new device architectures and pathways to on-chip photonic integration.[6] An essential component for a viable photonic circuit is a high-performance NW-based laser. Researchers have sought to make efficient NW-based lasers by a number of methods, including top-down photonic crystal (PhC) cavities,[7] microstadium resonators,[8] plasmonic waveguides,[9] and NWs that support whispering gallery modes.[10,11] So far, these demonstrations have largely been limited to single NWs due to lack of control over position and diameter, thus inhibiting low-loss optical cavity design with sufficient material gain,[12,13] while avoiding highly detrimental surface recombination.[14] In some cases, the resonant cavity and the NW active region require separate lithography and processing steps.[7,8] In other cases the cavity is simply limited by optical losses at the facets.[9−11] As a result, NW-laser demonstrations to date have large threshold power densities and awkward external coupling schemes making them impractical for large-scale integration. Typical reported values of threshold power density range from ~100 kW/cm^2 to >1 MW/cm^2 and require femtosecond pulses. Furthermore, most reported NW-based lasers are multimode, which can limit their utility for communications and multiplexing applications.

In order to overcome these problems and realize a practical NW-based laser solution, a high-Q cavity with effective surface passivation is necessary. Of the different possible candidates for high-Q optical cavities, PhC nanocavity resonators[15] are an attractive choice due to small mode volume,[16] high spontaneous emission coupling factor,[16,17] and low threshold power.[16,17] In this work, we implement a "bottom-up" technique where the PhC cavity is formed entirely by III−V NPs using catalyst-free selective-area metal−organic chemical vapor deposition.[18] The resulting device is fundamentally different in that it uses an NP ensemble rather than a single NW to form both active region and cavity. This approach is enabled by accurate control of position and diameter of the NPs, whereby the photonic band gap and active gain region are grown simultaneously from a masked substrate. By carefully engineering the geometry and heterostructures of the NPs forming the cavity, we achieve low-threshold single mode lasing at room-temperature.

The NPs forming the PhC lasers implement a GaAs/InGaAs/GaAs axial heterostructure for accurate placement of gain within the cavity,[19] while radial growth of InGaP shells provides in situ passivation. The selective-area grown NPs take the equilibrium shape determined by environmental growth conditions with the resulting side-wall facets consisting of the {1−10} family of crystal planes.[20] The resulting pillar sidewalls are perfectly vertical and have atomic scale roughness,[21,22] which inherently avoids two major contributions to loss in top-down PhC cavities.[23,24] Both pillar placement and diameter, which fix cavity resonance

Received: August 30, 2011
Revised: November 8, 2011

dx.doi.org/10.1021/nl2030163 | Nano Lett. XXXX, XXX, 000–000

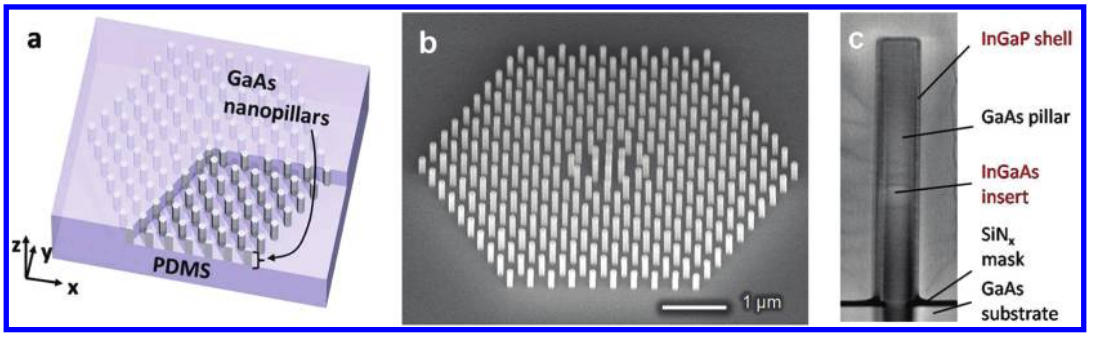

Figure 1. (a) Schematic diagram of the NP PhC lasers in PDMS. (b) A 45° tilted SEM of an NP PhC as grown on the substrate. (c) Cross-section STEM of an NP showing the InGaAs insert located at the center of the pillar and InGaP shell.

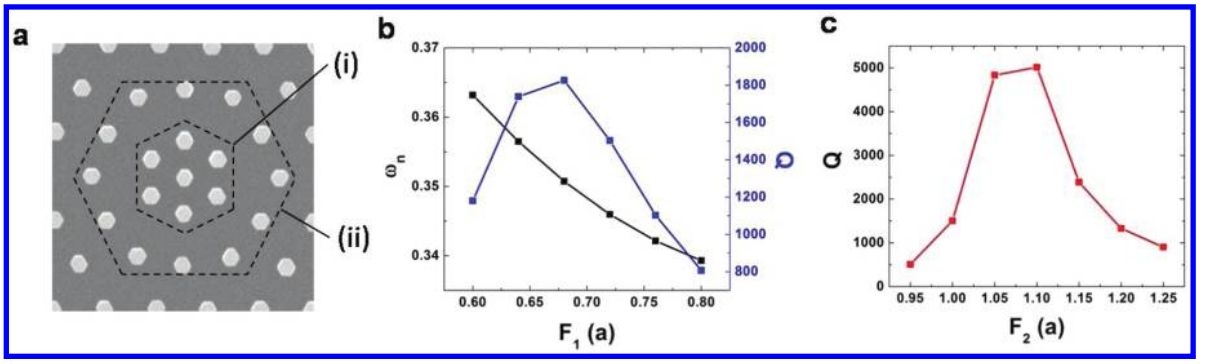

Figure 2. (a) Top-down SEM image of the NPs forming the high-Q cavity. The two hexagonal contours labeled (i) and (ii) show the regions where the NP positions were optimized. (b) The Q and frequency dependence on the NP spacing in region (i). (c) The Q dependence on the NP spacing in region (ii).

wavelength and Q, are determined lithographically. Thus, the cavity resonant wavelength can be designed arbitrarily. Furthermore, the same patterns used to define the position and diameter of the NPs also include optical alignment marks for device integration.

The bottom-up PhC lasers consist of NPs embedded in polydimethylsiloxane (PDMS) as shown in Figure 1a. The NPs are first grown on a SiN_x masked GaAs (111)B substrate. Following growth, PDMS is drop cast to a thickness of ~1 mm and cured in atmosphere. The PDMS film is then removed mechanically from the growth substrate. During the PDMS lift-off, the NPs are broken at the base making the patterned substrate reusable for additional growths. The resulting structure forms the complete laser cavity, where the NPs are surrounded by PDMS on all but the top side where they are exposed to air.

Figure 1b shows an SEM image of a typical NP PhC laser as grown on the substrate. Each device is a 5 μm × 5 μm array of hexagonally packed pillars that comprise the resonant cavity, surrounding seven central pillars which form the laser active region. The cavity Q and resonant wavelength are lithographically defined by NP diameter and pitch, respectively. A 4 × 6 matrix of cavity arrays is patterned across the growth substrate for controlled variation in both pillar diameter (100−130 nm) and interpillar pitch (324−342 nm). A microscope image of the device array matrix embedded in PDMS is shown in supporting material.

A cross-section scanning transmission electron microscope (STEM) image of a single representative NP from one of the cavities is shown in Figure 1c. The pillars are ~730 nm tall and 120 nm in diameter with about 5−10% height variation from center to edge of a cavity and are comprised of both an axial and a radial heterostructure. The axial double-heterostructure is formed by a well-placed 130 nm $In_xGa_{1-x}As$ insert, where x is measured to be ~15% from both the spontaneous emission peak wavelength and energy dispersive X-ray spectroscopy scan. The lateral heterostructure is formed by a 5 nm lattice-matched InGaP shell to reduce surface recombination. The details of the patterning process and growth conditions are described in more detail elsewhere.[18,19]

Three dimensional (3D) finite-difference time-domain (FDTD) simulations are employed to optimize structural parameters such as the height, radius, and the locations of the NPs. The cavity is formed by modifying the original lattice points of the triangular photonic-crystal as shown in Figure 2a. The cavity consists of two separate subregions defined by the two hexagonal contours labeled (i) and (ii). For the inner region (i), the six pillars are rotated by 90° with respect to the center pillar position. The distance is then scaled down from the center by a factor of F_1. Figure 2b shows the change in cavity Q and normalized resonant frequency ω_n as a function of F_1. It should be noted that Q and the frequency of the mode are critically dependent on F_1, since the majority of the mode energy is concentrated within these six pillars. For the outer region (ii), the twelve pillar positions are arranged in a circle and fine-tuned by the scaling factor F_2 to optimize Q as shown in Figure 2c.

A top-down and cross-sectional view of the electric-field intensity distribution ($|\mathbf{E}|^2$) in the cavity is shown in Figure 3a. The final arrangement of the NPs in the center of the cavity forms a nondegenerate hexapole mode.[25] The positions of the neighboring

dx.doi.org/10.1021/nl2030163 |Nano Lett. XXXX, XXX, 000–000

pillars are modified to maximize the cavity Q while keeping the resonant frequency close to the center of the PBG in order to maintain a large spontaneous emission factor β. The final result of this design optimization yields a simulated cavity Q of 4600 with an effective mode volume V_{eff} of 0.137 $(\lambda/n)^3$. In the cross-sectional view of Figure 3a, the location of the InGaAs inserts is highlighted to show the confinement of carriers to the field antinode. On the basis of the insert length as a fraction of the total pillar, the energy confinement factor Γ and threshold gain g_{th} are calculated with group index and material dispersion of bulk InGaAs.[26] With an insert length that is 18% of the total height as measured by STEM, this method yields $\Gamma = 0.185$ and $g_{\text{th}} = 197\ \text{cm}^{-1}$.

The devices are optically pumped using a pulsed semiconductor laser with a 660 nm peak wavelength, 10 μm diameter spot size, and 16 ns excitation pulse at a 1 MHz repetition rate. A 50× microscope objective oriented at 45° to the surface normal is used to both excite the NPs and collect emission. Simulated far-field radiation patterns[28] of the cavity resonant mode (Figure 2B) show that the laser emission should be directed 50−70° from normal. Figure 4a shows emission spectra from one array both below and above threshold at pump powers of $0.5 \times L_{\text{th}}$ and $2 \times L_{\text{th}}$. Below threshold, the spectrum is the integrated emission from all NPs within the array including cavity and active region. The spontaneous spectrum is peaked near 975 nm with FWHM of 65 nm. Even at this very low pump power, the resonant cavity mode can be detected. The characteristics of the subthreshold cavity emission has not yet been analyzed as stimulated or spontaneous. The FWHM of the modal peak is approximated to be 0.45 nm, which corresponds to an experimental cavity Q of ∼2000. At $2 \times L_{\text{th}}$, the spectrum is dominated by a single peak at 989 nm. The corresponding $L-L$ curve for this device, shown as the inset, indicates a lasing threshold of 500 μW peak pulse power or 625 W/cm^2 peak power density. The output power increases linearly until above $2 \times L_{\text{th}}$ where the device emission begins to saturate, reaching an estimated peak output power of 42.5 nW at the InGaAs detector.

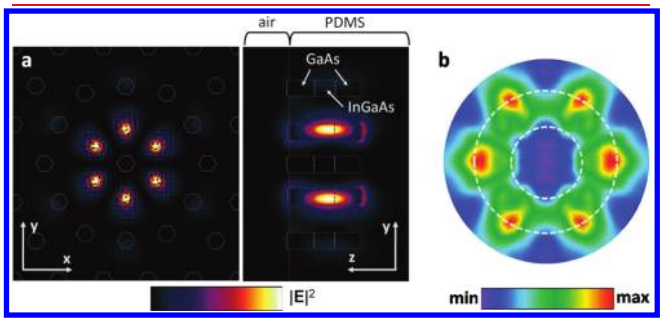

Figure 3. (a) Top-down view of the vector field pattern of the magnetic-field (H_x, H_y) overlaid upon the electric-field intensity ($|\mathbf{E}|^2$) distribution within the cavity showing the hexapole mode overlapping six center NPs and cross-section view of $|\mathbf{E}|^2$ within the cavity showing the overlap with the InGaAs inserts. (b) Far-field radiation pattern of the cavity hexapole mode. The far-field data over the upper hemispherical points (θ,ϕ) is represented in (x,y) by the mapping defined by $x = \theta \cos\phi$ and $y = \theta \sin\phi$.

The model used to predict the ideal Q required threshold gain gives $g_{\text{th}} = 197\ \text{cm}^{-1}$. However, with the measured cavity Q of ∼2000, an actual threshold gain of $g_{\text{th}} \sim 500\ \text{cm}^{-1}$ is predicted. Since InGaAs bulk gain can be expected to reach >1000 cm^{-1} at room temperature with moderate carrier densities,[14] the measured $L-L$ curve and consequent lasing threshold appear to be in reasonable agreement with the predictions of the model. This combined with the measured data provide strong evidence that the devices achieve single mode lasing at low threshold power density. Additionally, the fact that these estimates are based on gain in bulk InGaAs indicates the effectiveness of the InGaP shells used for surface passivation since the threshold for unpassivated InGaAs with the given surface to volume ratio would not be achievable at room temperature.

Figure 4b shows a comparison of three devices at $\sim 2 \times L_{\text{th}}$ that demonstrates the ability to control lasing wavelength lithographically. The devices A, B, and C are designed to have the cavity resonance at 950, 970, and 990 nm, which correspond to pillar pitch a of 324, 331, and 338 nm, respectively. This allows control of the wavelength with pitch by $d\lambda/da = 2.1$. However, the final height of the grown pillars does not match the target height from the optimized design due to both inaccuracy of the growth time of the pillars, as well as the difference in growth rate between devices due to difference in diameter. The resulting peak wavelengths are 960, 974, and 989 nm. A high-resolution scan of

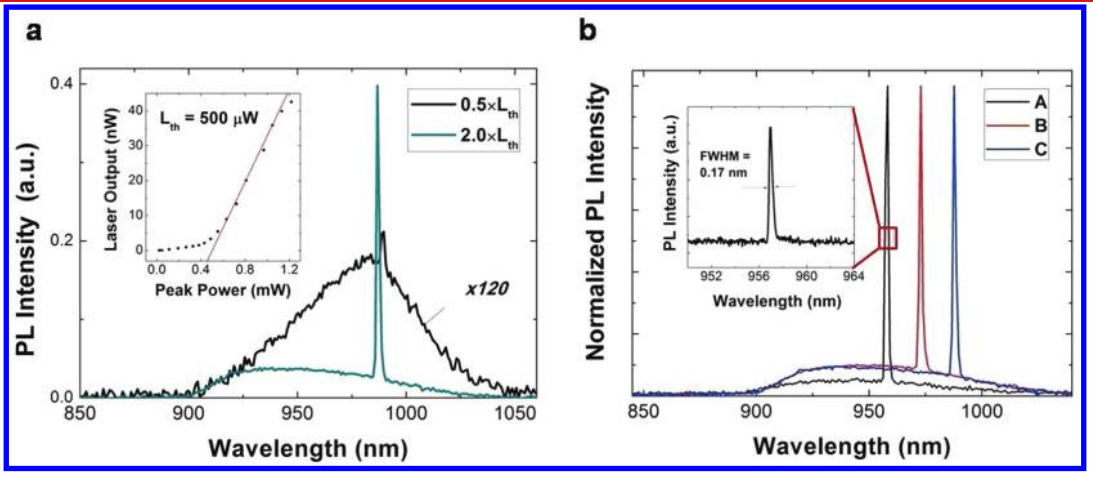

Figure 4. (a) Emission spectra of an NP PhC laser emitting at 989 nm both at $0.5 \times L_{\text{th}}$ and $2 \times L_{\text{th}}$. Inset shows $L-L$ curve of the same device with a threshold of 500 μW peak pulse power. (b) Comparison of devices A, B, and C with different pitch and diameter NPs that emit at wavelengths between 960 and 990 nm. Inset shows high-resolution laser spectrum of device A with a FWHM of 0.17 nm.

dx.doi.org/10.1021/nl2030163 |*Nano Lett.* XXXX, XXX, 000–000

the laser spectrum of device A, in the inset, shows a FWHM of 0.17 nm.

The bottom-up approach to NP PhC lasers introduces many design possibilities, which cannot be realized with the top-down PhC devices. On the basis of the measured threshold power density, we expect that further design optimization of the NP PhC cavities and increased InGaAs insert thickness will reduce the threshold gain by a factor of 4 or 5 to achieve continuous wave, room-temperature operation.[16,17] Additional modification of NP position and diameter within the cavity will enable engineering of the far-field emission pattern.[29,30] The current design featuring NPs embedded in PDMS can be useful as internal light sources for spectroscopy in microfluidic and biosensing systems,[27,28] especially since the patterned growth substrate can be reused after PDMS lift-off. In parallel, we are exploring on-chip integration utilizing a dielectric core-cladding stack to achieve out-of-plane optical confinement while the NPs remain on the growth substrate. Finally, with the narrow line width and lithographic control of wavelength, these devices are promising for on-chip wavelength division multiplexing applications.

■ ASSOCIATED CONTENT

Supporting Information. Additional information and figures. This material is available free of charge via the Internet at http://pubs.acs.org.

■ AUTHOR INFORMATION

Corresponding Author

*E-mail: (A.C.S) ascofield@ucla.edu; (D.L.H.) huffaker@ee.ucla.edu.

■ ACKNOWLEDGMENT

The authors gratefully acknowledge support from Dr. Gernot Pomrenke and Dr. Kitt Reinhardt of the Air Force Office of Scientific Research (Grant FA9550-08-1-0198), (Grant FA9550-09-1-0270), the National Science Foundation (Grant ECCS-0824273), (Grant DMR-1007051), and the United States Department of Defense (Grant NSSEFF N00244-09-1-0091). J.N.S. acknowledges support from the NSF Clean Energy for Green Industry IGERT (Grant DGE-0903720). Caltech authors would like to acknowledge support from the Defense Advanced Research Projects Agency under the Nanoscale Architecture for Coherent Hyperoptical Sources program (Grant W911NF-07-1-0277).

■ REFERENCES

(1) Kuykendall, T.; Ulrich, P.; Aloni, S.; Yang, P. *Nat. Mater.* **2007**, *6*, 951.
(2) Algra, R. E.; et al. *Nature* **2008**, *456*, 369.
(3) Lauhon, L. J.; Gudiksen, M. S.; Wang, D.; Lieber, C. M. *Nature* **2002**, *420*, 57.
(4) Martensson, T.; et al. *Nano Lett.* **2004**, *4*, 1987.
(5) Tomioka, K.; Motohisa, J.; Hara, S.; Fukui, T. *Nano Lett.* **2008**, *8*, 3475.
(6) Yan, R.; Gargas, D.; Yang, P. *Nat. Photonics* **2009**, *3*, 569.
(7) Heo, J.; Guo, W.; Bhattacharya, P. *Appl. Phys. Lett.* **2011**, *98*, 21110.
(8) Park, H.-G.; Qian, F.; Barrelet, C. J.; Li, Y. *Appl. Phys. Lett.* **2007**, *91*, 251115.
(9) Oulton, R. F.; Sorger, V. J.; Zentgraf, T.; Ma, R.-M.; Gladden, C.; Dai, L.; Bartal, G.; Zhang, X. *Nature* **2009**, *461*, 629.
(10) Gargas, D. J.; Moore, M. C.; Ni, A.; Chang, S.-W.; Zhang, Z.; Chuang, S.-L.; Yang, P. *ACS Nano* **2010**, *4*, 3270.
(11) Chen, R.; Tran, T.-T. D.; Ng, K. W.; Ko, W. S.; Chuang, L. C.; Sedgwick, F. G.; Chang-Hasnain, C. *Nat. Photonics* **2011**, *5*, 170.
(12) Ning, C. Z. *Phys. Status Solidi B* **2010**, *247*, 774.
(13) Li, D. B.; Ning, C. Z. *Phys. Rev. B* **2009**, *80*, 153304.
(14) Coldren, L.A.; Corzine, S. W. *Diode Lasers and Photonic Integrated Circuits*; Wiley: New York, 1995.
(15) Painter, O.; Lee, R. K.; Scherer, A.; Yariv, A.; O'Brien, J. D.; Dapkus, P. D.; Kim, I. *Science* **1999**, *284*, 1819.
(16) Nozaki, K.; Kita, S.; Baba, T. *Opt. Express* **2007**, *15*, 7506.
(17) Nomura, M.; Kumagai, N.; Iwamoto, S.; Ota, Y.; Arakawa, Y. *Opt. Express* **2009**, *17*, 15975.
(18) Scofield, A. C.; Shapiro, J. N.; Lin, A.; Williams, A. D.; Wong, P-S; Liang, B. L.; Huffaker, D. L. *Nano Lett.* **2011**, *11*, 2242.
(19) Shapiro, J. N.; Lin, A.; Wong, P. S.; Scofield, A. C.; Tu, C.; Senanayake, P. N.; Mariani, G.; Liang, B. L.; Huffaker, D. L. *Appl. Phys. Lett.* **2010**, *97*, 243102.
(20) Ikejiri, K.; Sato, T.; Yoshida, H.; Hiruma, K.; Motohisa, J.; Hara, S.; Fukui, T. *Nanotechnology* **2008**, *19*, 265604.
(21) Tomioka, K.; Motohisa, J.; Hara, S.; Fukui, T. *Jpn. J. Appl. Phys.* **2007**, *46*, 1102.
(22) Noborisaka, J.; Motohisa, J.; Fukui, T. *Appl. Phys. Lett.* **2005**, *86*, 213102.
(23) Johnson, S. G.; Fan, S.; Villeneuve, P. R.; Joannopoulos, J. D.; Kolodziejski, L. A. *Phys. Rev. B* **1999**, *60*, 5751.
(24) Tanaka, Y.; Asano, T.; Akahane, Y.; Song, B.-S.; Noda, S. *Appl. Phys. Lett.* **2003**, *82*, 1661.
(25) Ryu, H.-Y.; Notomi, M.; Lee, Y.-H. *Appl. Phys. Lett.* **2003**, *83*, 4294.
(26) Chang, S.-W.; Lin, T.-R.; Chuang, S. L. *Opt. Express* **2010**, *18*, 15039.
(27) Loncar, M.; Scherer, A.; Qiu, Y. *Appl. Phys. Lett.* **2003**, *82*, 4628.
(28) Kim, S.-H.; Choi, J.-H.; Lee, S.-K.; Kim, S.-H.; Yang, S.-M.; Lee, Y.-H.; Seassal, C.; Regrency, P.; Viktorovitch, P. *Opt. Express* **2008**, *16*, 6515.
(29) Kim, S.-H.; Kim, S.-K.; Lee, Y.-H. *Phys. Rev. B* **2006**, *73*, 235117.
(30) Tran, N.-V.-Q.; Combrie, S.; Rossi, A. D. *Phys. Rev. B* **2009**, *79*, 041101.